

A Directional Gradient-Curvature Method for Gap Filling of Gridded Environmental Spatial Data with Potentially Anisotropic Correlations

Milan Žukovič^{a,b}, Dionissios T. Hristopoulos^{c,*}

^a*Institute of Physics, Faculty of Science, Pavol Jozef Šafárik University, Park Angelinum 9, 040 01 Košice, Slovakia*

^b*SORS Research a.s., Moyzesova 38, 040 01 Košice, Slovakia*

^c*Geostatistics Research Unit, Department of Mineral Resources Engineering, Technical University of Crete, Chania 73100, Greece*

Abstract

We introduce the Directional Gradient-Curvature (DGC) method, a novel approach for filling gaps in gridded environmental data. DGC is based on an objective function that measures the distance between the directionally segregated normalized squared gradient and curvature energies of the sample and entire domain data. DGC employs data-conditioned simulations, which sample the local minima configuration space of the objective function instead of the full conditional probability density function. Anisotropy and non-stationarity can be captured by the local constraints and the direction-dependent global constraints. DGC is computationally efficient and requires minimal user input, making it suitable for automated processing of large (e.g., remotely sensed) spatial data sets. Various effects are investigated on

*Corresponding author.

Email addresses: milan.zukovic@upjs.sk (Milan Žukovič), dionisi@mred.tuc.gr (Dionissios T. Hristopoulos)

URL: <http://www.mred.tuc.gr/home/hristopoulos/dionisi.htm> (Dionissios T. Hristopoulos)

synthetic data. The gap-filling performance of DGC is assessed in comparison with established classification and interpolation methods using synthetic and real satellite data, including a skewed distribution of daily column ozone values. It is shown that DGC is competitive in terms of cross validation performance.

Keywords: correlation, anisotropy, spatial interpolation, stochastic estimation, optimization, simulation

1. Introduction

Atmospheric data, whether they are obtained by means of ground or remote sensing methods, often include data gaps. Such gaps arise due to different reasons, e.g. incomplete time series, spatial irregularities of sampling pattern, equipment limitations or sensor malfunctions (Jun & Stein, 2004; Lehman et al., 2004; Albert et al., 2012; Bechle et al., 2013). For example, remote sensing images may include obscured areas due to cloud cover, whereas gaps also appear between satellite paths where there is no coverage for a specific period (Emili et al., 2011). The impact of missing data on the estimate of statistical averages and trends can be significant (Sickles & Shadwick, 2007). There is an interest in the development of new methods for filling gaps in atmospheric data and their comparison with existing imputation methods (Junninen et al., 2004). Particularly for frequently collected, massive remotely sensed data, the efficient filling of the gaps is a challenging task. Traditional geostatistical interpolation methods such as kriging, e.g. (Wackernagel, 2003), can be impractical due to high computational complexity, restriction to Gaussian data, as well as var-

18 ious subjective choices in variogram modeling and interpolation search ra-
 19 dius (Diggle & Ribeiro, 2007). In particular, computationally efficient meth-
 20 ods are needed for filling gaps in very large data sets (Cressie, 2008; Hartman & Hössjer,
 21 2008).

22 In the following, we consider a set of sampling points $G_s = \{\vec{s}_i, i =$
 23 $1, \dots, N\}$, where $\vec{s}_i = (x_i, y_i) \in \mathbb{R}^2$. The points are scattered on a rect-
 24 angular grid \tilde{G} of size $N_G = L_x \times L_y$, where L_x and L_y are respectively
 25 the horizontal and vertical dimensions of the rectangle (in terms of the unit
 26 length), such that $N_G > N$. Let $G_p = \{\vec{s}_p, p = 1, \dots, P\}$ be the set of predic-
 27 tion points, representing locations of missing values, such that $\tilde{G} = G_s \cup G_p$.
 28 The data, $\mathbf{Z}(G_s) = \{z_i, \forall \vec{s}_i \in G_s\}$, are considered as a realization of the con-
 29 tinuous random field $Z(\vec{s}_i)$. To reduce the dimensionality of the configuration
 30 space, we discretize the continuously valued field. For applications that do
 31 not require high resolution, e.g. environmental monitoring and risk manage-
 32 ment, $\mathbf{Z}(G_s)$ can be discretized into a small (e.g., eight) number N_c of levels
 33 (classes). Continuous distributions are obtained at the limit $N_c \rightarrow \infty$. In the
 34 current study, the spatial prediction of missing values is posed as a spatial
 35 classification problem for ranked numerical data. Continuous interpolation
 36 is approximated by considering an arbitrarily high number of levels.

37 The discretization classes $\mathcal{C}_q, q = 1, \dots, N_c$ correspond to the intervals
 38 $\mathcal{C}_q = (t_q, t_{q+1}]$ for $q = 2, \dots, N_c - 1$, $\mathcal{C}_1 = (-\infty, t_2]$, and $\mathcal{C}_{N_c} = (t_{N_c}, \infty)$. The
 39 classes are defined with respect to threshold levels $t_k, k = 2, \dots, N_c$. All the
 40 classes have a uniform width except \mathcal{C}_1 and \mathcal{C}_{N_c} which extend to negative
 41 and positive infinity respectively, to include values outside the observed in-
 42 terval $[z_{\min}, z_{\max}]$. More general class definitions can be investigated. The

43 *class identity field* $I(\vec{s})$ takes integer values $q = 1, \dots, N_c$ that represent the
 44 respective class index. In particular, $I(\vec{s}_i) = q$ implies that $z_i \in \mathcal{C}_q$. The
 45 prediction problem is equivalent to assigning a class label at each point in
 46 G_p . A map of the process Z can be generated consisting of equivalent-class
 47 (isolevel) contours.

48 2. The Directional Gradient-Curvature Model

49 The Directional Gradient-Curvature (DGC) model is inspired by Spar-
 50 tan spatial random fields (SSRF) (Hristopulos, 2003), which are based on
 51 short-range interactions between the field values. The SSRF model is para-
 52 metric and represents stationary, continuous and isotropic Gaussian random
 53 fields. To relax these assumptions, we introduce an almost non-parametric
 54 approach that aims at matching short-range correlations in G_s with those of
 55 \tilde{G} . This idea was recently successfully applied to spatial random fields still
 56 assuming spatial isotropy (Žukovič & Hristopulos, 2012). The present model
 57 extends this approach by relaxing even the isotropic assumption through in-
 58 corporating anisotropic dependence. In particular, the correlations used in
 59 DGC represent the normalized squared gradient and curvature energies of
 60 the discretized class identity field along different directions. Let a_n be the
 61 lattice step in direction \vec{e}_n . The local square gradient and curvature terms
 62 in each of the d directions used are given by

$$G_n(I; \vec{s}_i) = \frac{[I(\vec{s}_i + a_n \vec{e}_n) - I(\vec{s}_i)]^2}{a_n^2}, \quad n = 1, \dots, d \quad (1)$$

$$C_n(I; \vec{s}_i) = \frac{[I(\vec{s}_i + a_n \vec{e}_n) + I(\vec{s}_i - a_n \vec{e}_n) - 2I(\vec{s}_i)]^2}{a_n^4}, \quad n = 1, \dots, d. \quad (2)$$

63 The normalized squared gradient, $\overline{G}_n(\mathbf{I}_g)$, and curvature, $\overline{C}_n(\mathbf{I}_g)$ energies
64 in a direction \vec{e}_n , are defined as averages of the above over the grid \tilde{G} . $\mathbf{I}_g =$
65 $[I(\vec{s}_1) \dots I(\vec{s}_{N_G})] \forall \vec{s}_i \in \tilde{G}$, represents the values of the class identity field
66 on the entire grid, $\mathbf{I}_p = [I(\vec{s}_1) \dots I(\vec{s}_P)] \forall \vec{s}_i \in G_p$, is the class field at the
67 prediction sites, and $\mathbf{I}_s = [I(\vec{s}_1) \dots I(\vec{s}_N)] \forall \vec{s}_i \in G_s$ are the class identity
68 values at the sampling sites. The matching of the gradient and curvature
69 constraints on G_s and \tilde{G} is based on the following *objective functional*:

$$U(\mathbf{I}_p | \mathbf{I}_s) = \sum_{n=1}^d [w_1 \phi(\overline{G}_n(\mathbf{I}_g), \overline{G}_n(\mathbf{I}_s)) + w_2 \phi(\overline{C}_n(\mathbf{I}_g), \overline{C}_n(\mathbf{I}_s))], \quad (3)$$

$$\phi(x, x') = \begin{cases} (1 - x/x')^2, & x' \neq 0 \\ x^2, & x' = 0. \end{cases} \quad (4)$$

70 In the above, $w = (w_1, w_2)$ represent gradient and curvature weights
71 ($w_1, w_2 \geq 0$, $w_1 + w_2 = 1$), and d is the number of the directions used.
72 We use (4) to measure the deviation between the G_s - and \tilde{G} -based val-
73 ues instead of $\phi = (x - x')^2$, because the gradient and curvature can have
74 very different magnitudes, depending on the units used; this means that one
75 term may dominate in the optimization. By using normalized constraints we
76 compensate for the possible disparity of magnitudes between gradient and
77 curvature. If one of the sample quantities is zero, the second line of (4) is

78 used to avoid a singular denominator.

79 We select $w = (0.5, 0.5)$ and $d = 4$, representing four directions with the
80 following angles (with respect to the positive x-axis): 0° , 45° , 90° , and 135° .
81 Given the above, the classification problem is equivalent to determining the
82 optimal configuration $\hat{\mathbf{I}}_p$ that corresponds to the minimum of (3):

$$\hat{\mathbf{I}}_p = \arg \min_{\mathbf{I}_p} U(\mathbf{I}_p | \mathbf{I}_s). \quad (5)$$

83 The optimization of (3) is conducted numerically. The choice of the initial
84 configuration is important to obtain a reliable, fast and automatic algorithm:
85 it should prevent the optimization from getting trapped in poor local minima
86 and minimize the relaxation path in configuration space to the equilibrium,
87 and it should also minimize the need for user intervention. The sampling
88 points retain their values \mathbf{I}_s . Assuming a certain degree of spatial continuity,
89 common in geospatial data sets, the initial state of \mathbf{I}_p is determined based on
90 the sample states in the immediate neighborhood of the individual prediction
91 points. The neighborhood of \vec{s}_p is determined by an $m \times m$ stencil ($m = 2l + 1$)
92 centered at \vec{s}_p . Then, the initial value at a prediction point is assigned by
93 majority rule, based on the prevailing value of its sample neighbors inside the
94 stencil. The stencil size is chosen automatically, reflecting the local sampling
95 density and the distribution of *class identity* values. Namely, it is adaptively
96 set to the smallest size that contains a finite number of sampling points with
97 a prevailing value. If no majority is reached up to some neighborhood size
98 $m_{\max} \times m_{\max}$, the initial value is assigned (i) randomly from the range of the
99 labels with tie votes or (ii) from the entire range of labels $1, \dots, N_c$, if majority
100 is not reached due to absence of sampling points within the maximum stencil.

101 The above method of initial state assignment will be referred to as majority
102 rule with adaptable stencil size (MRASS).

103 The updating of class identity states on G_p uses the “greedy” Monte Carlo
104 (MC) method (Papadimitriou & Steiglitz, 1982), which unconditionally ac-
105 cepts a new state if the latter lowers the cost function. The greedy MC
106 algorithm may cause the termination of the DGC algorithm at local minima
107 of the objective function (3). Targeting exclusively global minima (e.g. by
108 simulated annealing) unduly emphasizes exact matching of the energies on
109 the entire domain with those in the sample domain; however, the latter are
110 subject to sampling fluctuations and measurement errors.

111 The algorithm performs a random walk through the grid G_p . It terminates
112 if P consecutive update trials do not produce a single successful update. If
113 the computational budget is a concern, the algorithm can terminate when a
114 pre-specified maximum number of Monte Carlo steps is exceeded. In either
115 case, the generated realization is accepted only if the residual value of the cost
116 function is below a user-defined tolerance level tol . Otherwise, the realization
117 is rejected and a new one is generated. The algorithm generates M different
118 realizations. The median values from all the accepted realizations at each
119 missing-value point represent the prediction of the algorithm. Associated
120 confidence intervals are also derived.

121 The main steps of the procedure described above are summarized by
122 means of the following algorithm.

- 123 1. Define the number of realizations M , the number of classes N_c , the
124 maximum stencil size m_{\max} , the residual cost function tolerance tol
125 and the maximum number of Monte Carlo steps i_{\max} (optional).

- 126 2. Discretize $\mathbf{Z}(G_s)$ to obtain the sample *class identity field* \mathbf{I}_s .
- 127 3. Calculate the directional sample energies $\overline{G}_n(\mathbf{I}_s), \overline{C}_n(\mathbf{I}_s), n = 1, \dots, d$.¹
- 128 4. Initialize the simulated realization index $j = 1$.
- 129 5. **while** $j \leq M$ repeat the following steps:
- 130 (a) Assign initial values $\hat{\mathbf{I}}_p^{(0)}$ to the prediction points in G_p based on
- 131 MRASS.
- 132 (b) Calculate the initial energy values $\overline{G}_n(\mathbf{I}_g^{(0)}), \overline{C}_n(\mathbf{I}_g^{(0)}), n = 1, \dots, d$,
- 133 and the objective function $U^{(0)} = U(\hat{\mathbf{I}}_p^{(0)}|\mathbf{I}_s)$.
- 134 (c) Initialize the simulated state index $i = 0$, and the rejected states
- 135 index $i_r = 0$.
- 136 (d) **while** $(i_r < P) \wedge (i \leq i_{\max})$ repeat the following updating steps:
- 137 i. Generate a new state $\hat{\mathbf{I}}_p^{(i+1)}$ by randomly, i.e., with probability
- 138 0.5, adding ± 1 to the state $\hat{\mathbf{I}}_p^{(i)}$, maintaining the condition
- 139 $1 \leq \hat{I}^{(i+1)}(\vec{s}_j) \leq N_c, \forall \vec{s}_j \in G_p$.
- 140 ii. Calculate $\overline{G}_n(\mathbf{I}_g^{(i+1)}), \overline{C}_n(\mathbf{I}_g^{(i+1)}), n = 1, \dots, d$.
- 141 iii. Calculate $U^{(i+1)} = U(\hat{\mathbf{I}}_p^{(i+1)}|\mathbf{I}_s)$.
- 142 iv. **If** $U^{(i+1)} < U^{(i)}$ accept the new state $\hat{\mathbf{I}}_p^{(i+1)}$; $i_r \rightarrow 0$;
- 143 **else** $\hat{\mathbf{I}}_p^{(i+1)} = \hat{\mathbf{I}}_p^{(i)}$; $U^{(i+1)} = U^{(i)}$; $i_r \rightarrow i_r + 1$; **end**.
- 144 v. $i \rightarrow i + 1$;
- 145 **end while**
- 146 (e) **If** $U^{(i)} < tol$ store the realization $\hat{\mathbf{I}}_p^*(j) = \hat{\mathbf{I}}_p^{(i)}$; $j = j + 1$;
- 147 **else** return to 5 (a); **end**.
- 148 **end while**

¹ The algorithm checks if the number of samples for calculating $\overline{G}_n(\mathbf{I}_s), \overline{C}_n(\mathbf{I}_s)$ is sufficient for obtaining reliable estimates.

149 6. Evaluate the statistics from the realizations $\hat{\mathbf{I}}_p^*(j)$, $j = 1, \dots, M$.

150 The DGC method lies between interpolation and conditional simulation.
151 Interpolation methods provide a single optimal configuration of the miss-
152 ing values, e.g., kriging is based on the minimization of the mean square
153 error. Conditional simulation based on Markov Chain Monte Carlo meth-
154 ods aims to sample the entire configuration space and reconstruct the joint
155 conditional probability density function of the missing data. DGC on the
156 other hand samples the configuration space that corresponds to local min-
157 ima of the objective function. Since DGC returns multiple realizations, we
158 can characterize it as a stochastic method. However, in DGC the sampling
159 of the configuration space is restricted to the subspace of local minima. The
160 afforded dimensionality reduction is responsible for the computational effi-
161 ciency of the method.

162 3. DGC validation methodology

163 In this section we conduct numerical experiments, in which a portion of
164 the data is set aside to be used for validation of the classification/interpolation
165 algorithms tested. The performance of DGC is evaluated by calculating the
166 misclassification rate $F^* = 1/P \sum_{\vec{s}_p \in G_p} \left[1 - \delta(I(\vec{s}_p), \hat{I}(\vec{s}_p)) \right]$, where $I(\vec{s}_p)$ is
167 the true class identity value at the validation points, $\hat{I}(\vec{s}_p)$ is the classifica-
168 tion estimate and $\delta(I, I') = 1$ if $I = I'$, $\delta(I, I') = 0$ if $I \neq I'$. The gap-filling
169 of DGC is compared with the k -nearest neighbor (KNN) (Dasarathy, 1991)
170 and fuzzy k -nearest neighbor (FKNN) (Keller et al., 1985) classification al-
171 gorithms. We chose the k values that minimize the cross validation errors
172 to obtain the lowest achievable errors by KNN and FKNN. The KNN and

173 FKNN algorithms are applied using the Matlab® function `fknn` (Akbas,
174 2007).

175 The interpolation performance is compared with the inverse distance
176 weighted (ID) (Shepard, 1968), nearest neighbors (NN), bilinear (BL), bicu-
177 bic (BC), and biharmonic spline (BS)(Sandwell, 1987) methods. For the
178 Gaussian synthetic data we also include the ordinary kriging (OK) method (Wackernagel,
179 2003). Given the Gaussian distribution and knowledge of the covariance pa-
180 rameters, OK provides optimal predictions and thus also a standard for com-
181 paring DGC estimates. The NN, BL, BC and BS interpolation algorithms
182 were implemented by means of the Matlab® function `griddata`. For ID we
183 used the Matlab® function `fillnans` (Howat, 2007). Finally, for OK we
184 used the routines available in the Matlab® library `vebyk` (Sidler, 2009).

185 Let $\hat{Z}(\vec{s}_p)$ be the estimate of the continuous field calculated from the back
186 transformation

$$\hat{Z}(\vec{s}_p) = [t_{\hat{I}_Z(\vec{s}_p)} + t_{\hat{I}_Z(\vec{s}_p)+1}]/2, \quad p = 1, \dots, P. \quad (6)$$

187 If $Z(\vec{s}_p)$ is the true value at \vec{s}_p the estimation error is $\epsilon(\vec{s}_p) = Z(\vec{s}_p) - \hat{Z}(\vec{s}_p)$.
188 For $N_c \gg 1$ we calculate the following prediction errors: average absolute
189 error

$$\text{AAE} = (1/P) \sum_{\vec{s}_p \in G_p} |\epsilon(\vec{s}_p)|, \quad (7)$$

190 average relative error

$$\text{ARE} = (1/P) \sum_{\vec{s}_p \in G_p} \epsilon(\vec{s}_p)/Z(\vec{s}_p), \quad (8)$$

191 average absolute relative error

$$\text{AARE} = (1/P) \sum_{\vec{s}_p \in G_p} |\epsilon(\vec{s}_p)|/Z(\vec{s}_p), \quad (9)$$

192 root average squared error

$$\text{RASE} = \sqrt{\sum_{\vec{s}_p \in G_p} (1/P) \epsilon^2(\vec{s}_p)}, \quad (10)$$

193 and linear correlation coefficient R .

194 If S sample configurations are considered, the mean values of the vali-
195 dation measures (i.e., the MAAE, MARE, MAARE, MRASE, and MR) are
196 calculated by averaging over the sample configurations. To focus on the lo-
197 cal performance of DGC, we use the respective “local” errors, i.e., MAE,
198 MRE, MARE, and RMSE, in which the spatial average is replaced by the
199 mean over predictions obtained from M different simulations. Furthermore,
200 we record the optimization CPU time, T_{cpu} , and the number of Monte Carlo
201 steps (MCS).

202 The computations are performed in Matlab® programming environment
203 on a desktop computer with 3.25 GB RAM and an Intel®Core™2 Quad
204 CPU Q9650 processor with an 3 GHz clock.

205 4. Results

206 4.1. Synthetic Data

207 DGC performance is first studied on synthetic data sampled on regu-
208 lar grids. The data are simulated from the Gaussian random field $Z \sim$

Table 1: Mean misclassification rate $\langle F^* \rangle$ [%] and standard deviation S_{F^*} for synthetic Gaussian data with anisotropic Matérn covariance obtained by the DGC, KNN and FKNN algorithms.

Levels	$N_c = 8$						$N_c = 16$					
p [%]	33			66			33			66		
Model	DGC	KNN	FKNN	DGC	KNN	FKNN	DGC	KNN	FKNN	DGC	KNN	FKNN
$\langle F^* \rangle$	18.9	29.1	27.5	26.9	35.6	34.8	26.4	51.4	51.4	38.6	58.1	57.9
S_{F^*}	1.6	1.4	1.4	2.2	1.2	1.2	2.1	1.6	1.5	2.5	1.1	1.0

209 $N(m = 50, \sigma = 10)$ with Whittle-Matérn covariance given by $c_Z(\vec{r}) =$
 210 $\sigma^2 \frac{2^{1-\nu}}{\Gamma(\nu)} h^\nu K_\nu(h)$, where $h = \sqrt{r_1^2/\xi_1^2 + r_2^2/\xi_2^2}$ and $\vec{r} = (r_1, r_2)$ is the lag dis-
 211 tance between two points. K_ν is the modified Bessel function of the second
 212 kind and of order ν , where $\nu = 2.5$ is the covariance smoothness parameter.
 213 The principal axes of anisotropy are aligned with the coordinate axes. The
 214 correlation length in the vertical direction is set to $\xi_2 = 2$ and in the hor-
 215 izontal direction to $\xi_1 = 4$. The field is sampled on a square grid \tilde{G} , with
 216 $N_G = 50 \times 50$ nodes using the spectral method (Drummond and Horgan,
 217 1987). Missing data samples $\mathbf{Z}(G_s)$ of size $N = N_G - \lfloor (p/100\%) N_G \rfloor$ are
 218 generated from the complete sets by randomly removing $P = \lfloor (p/100\%) N_G \rfloor$
 219 values, which are used as validation points. For different degrees of thinning
 220 (typically $p = 33\%$ and 66%), we generate $S = 100$ different sampling config-
 221 urations. The predictions at the removed points are calculated and compared
 222 with the true values.

223 The classification results for the synthetic data are summarized in Table 1.
 224 The misclassification rate obtained by DGC is considerably smaller than the
 225 KNN and FKNN rates in all cases, although DGC shows somewhat larger
 226 sample-to-sample fluctuations. The mean CPU time required by DGC ranges
 227 between 0.96 and 1.11 seconds and the mean number of Monte Carlo steps

228 between 10^4 and 5×10^4 . The DGC interpolation performance is evaluated in
 229 Table 2 using $N_c = 1000$ classes. In terms of validation errors (smallest errors
 230 and largest R), for the uniformly thinned data ($p = 33\%$, 66%) OK ranked
 231 best. As mentioned above, for Gaussian data with known covariance pa-
 232 rameters OK is expected to give optimal predictions. The known directional
 233 correlation lengths also allowed identifying a region of influence around the
 234 prediction points, thus optimizing search neighborhoods and consequently
 235 the OK CPU time. Nevertheless, the OK CPU time was the highest. For
 236 $p = 33\%$ the DGC performance ranked second and for $p = 66\%$ it was com-

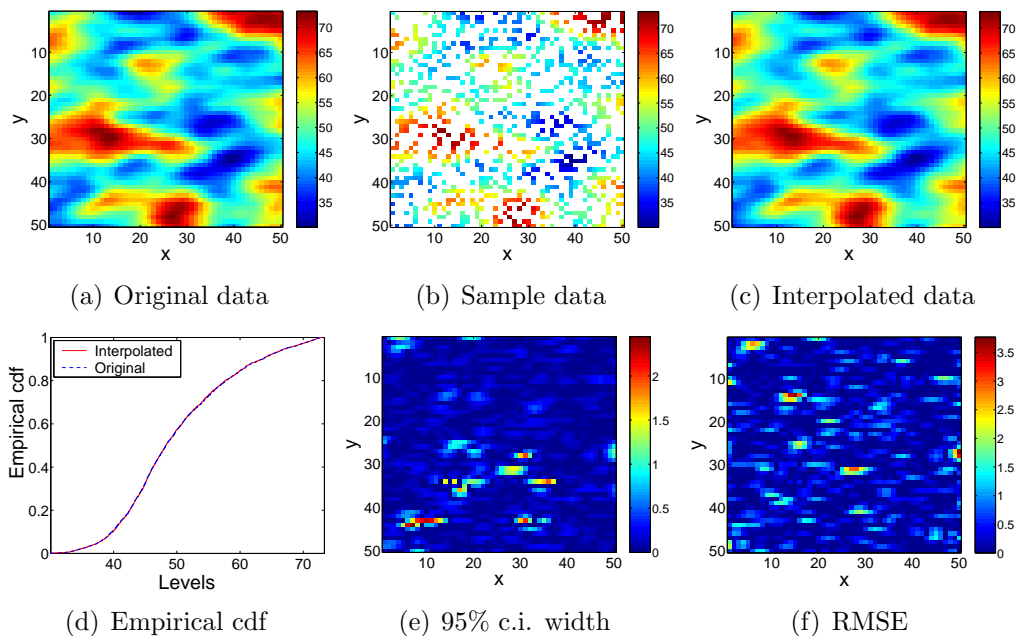


Figure 1: DGC interpolation results for synthetic Gaussian data with anisotropic Matérn covariance based on $M = 100$ simulation runs on a single sample generated by 66% thinning. Subfigures include (a) original field, (b) thinned sample, (c) interpolated data based on the median values from M runs, (d) comparison of the empirical cdfs of the original and interpolated data, (e) spatial distribution of the 95% confidence interval (c.i.) widths, and (f) root mean squared errors of predictions.

237 parable to BS, with the other models performing worse than DGC. We note
238 that DGC values in Tables 1 and 2 are based on $M = 1$ simulation run for
239 each of $S = 100$ sample realizations. Increased values of M (e.g. $M = 100$)
240 only marginally improved the validation results.

241 To account for more realistic patterns of missing data in remote sensing,
242 e.g. due to cloud cover, we investigate a sample realization in which a solid
243 block of data (rectangle of 16×8 pixels) is missing (see Fig. 2). The block
244 is deliberately chosen to include a small area with extreme values to test the
245 ability of DGC to predict a “hotspot”. For this study, DGC performs better
246 than the other methods. To compensate for using one sample ($S = 1$), we
247 run $M = 100$ simulations. Therefore the DGC CPU time is considerably
248 higher compared to the (a) and (b) cases ($M = 1$).

249 The dramatic increase of the OK CPU time is caused by the augmented
250 search neighborhood necessary to span the missing data gap and the cubic
251 dependence of kriging on the number of points in the search neighborhood.
252 Generally, the DGC CPU time is proportional to N_c and increases with p ,
253 reflecting the increased dimension of the configuration space and number
254 of variables involved in the optimization. For $p = 66\%$ the optimization
255 involves approximately 10^6 Monte Carlo steps. As shown in Fig. 1, multiple
256 simulation runs allow estimating the interpolation uncertainty, with respect
257 to the subspace of configurations that correspond to local minima of the
258 objective function (3).

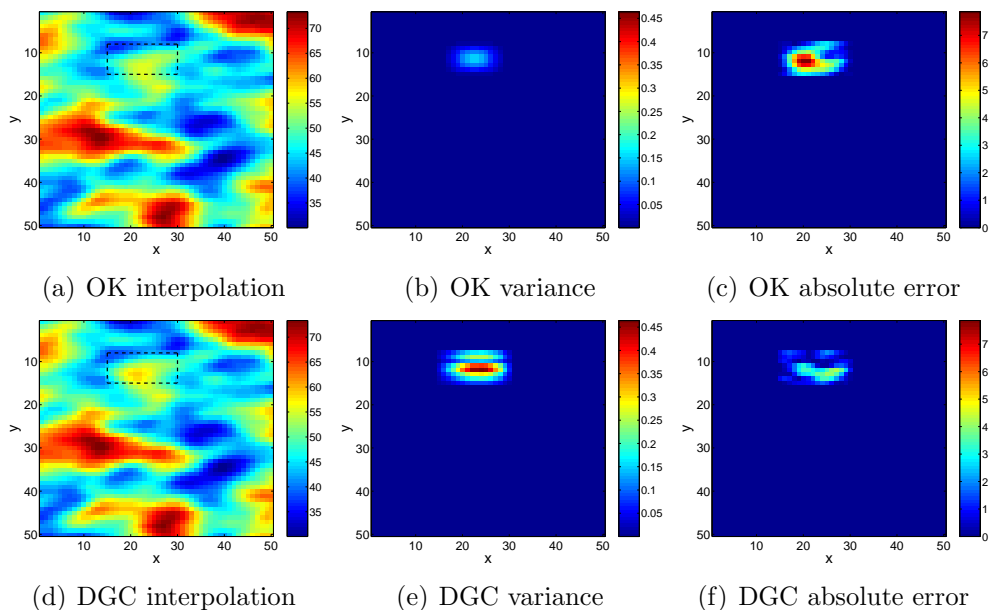


Figure 2: Interpolation results for synthetic Gaussian data with anisotropic Matérn covariance. Sample data are generated by removal of a block of data in the area marked by the dashed rectangle. The DGC results are based on $M = 100$ simulation runs. Subfigures show data interpolated by (a) OK and (d) DGC, variance by (b) OK and (e) DGC, and absolute errors by (c) OK and (f) DGC.

259 *4.2. Real Data*

260 *4.2.1. Radioactive Potassium Concentration*

261 The first real data set represents soil concentration of radioactive potas-
 262 sium measured by gamma-ray spectrometry over part of Canada (Anonymous,
 263 2008), on a grid with $N_G = 256 \times 256$ nodes extending in latitude from 56S to
 264 57N and in longitude from -100 W to -98 E, with a resolution of 250 m. The
 265 data have been preprocessed to correct for background and airplane flight
 266 height. The potassium concentrations are in units of % and their summary
 267 statistics are as follows: $N_G = 65536$, $z_{\min} = 0.39$, $z_{\max} = 3.26$, $\bar{z} = 1.60$,
 268 $z_{0.50} = 1.61$, $\sigma_z = 0.52$, skewness coefficient equal to 0.10, and kurtosis coef-

Table 2: Interpolation validation measures for Gaussian data with anisotropic Matérn covariance, using (a,b) $S = 100$ samples generated by 33% and 66% random thinning, respectively, and (c) $S = 1$ sample generated by removal of a solid block of data. The DGC uses $N_c = 1000$ and the results are based on $M = 1$ simulation run in (a) and (b) and $M = 100$ simulation runs in (c).

	MAAE			MARE [%]			MAARE [%]			MRASE			MR [%]			$\langle T_{cpu} \rangle$		
	(a)	(b)	(c)	(a)	(b)	(c)	(a)	(b)	(c)	(a)	(b)	(c)	(a)	(b)	(c)	(a)	(b)	(c)
DGC	0.17	0.50	1.28	-0.01	-0.07	1.70	0.35	1.04	2.45	0.33	0.83	1.71	99.93	99.56	98.84	3.16	8.78	166
NN	2.08	2.09	5.01	-0.19	-0.17	8.12	4.25	4.26	9.77	2.65	2.73	6.24	95.61	95.35	75.52	0.04	0.02	0.08
BL	0.63	1.01	4.95	-0.12	-0.21	6.49	1.29	2.10	9.41	0.91	1.51	6.07	95.59	95.30	75.52	0.04	0.02	0.06
BC	0.43	0.78	4.92	-0.06	-0.12	6.82	0.89	1.61	9.32	0.65	1.21	6.09	99.74	99.09	79.00	0.04	0.02	0.06
BS	0.32	0.55	5.09	-0.02	-0.06	9.19	0.65	1.13	9.61	0.41	0.78	6.30	99.90	99.62	83.45	2.06	0.57	0.49
ID	1.04	1.44	5.14	-0.29	-0.33	7.33	2.15	2.96	9.85	1.34	1.91	6.22	99.09	97.84	77.06	0.16	0.17	0.06
OK	0.06	0.31	2.49	-1E-5	-0.01	4.66	0.12	0.65	4.71	0.12	0.49	3.19	99.99	99.85	96.75	31.1	9.15	2546

269 ficient equal to 2.45. A plot of the data in Fig. 3(a) displays clear signs of
 270 anisotropy. Samples $\mathbf{Z}(G_s)$ were generated from the original data by random
 271 thinning with $p = 33\%$ and 66% .

272 Classification ($N_c = 8, 16$) and interpolation ($N_c = 1500$) results for
 273 $p = 33\%$ are listed in Table 3. The prediction performance of DGC is su-
 274 perior to other models except for the BS. The outstanding performance of
 275 the latter is likely due to the smooth spatial variation of the radioactivity
 276 data. An example of prediction results based on $M = 100$ simulation runs
 277 for one sample realization with $p = 66\%$ is shown in Fig. 3. The DGC clas-
 278 sification CPU time with $N_c = 8, 16$ was 2.6 and 3.3 seconds respectively.
 279 The computational time for DGC interpolation is comparable to that of BS,
 280 but one order higher than NN, BL, and BC times. The limiting factor in
 281 DGC are the MC simulations that involve up to $\sim 10^7$ Monte Carlo steps
 282 (see Fig. 4(a)). The histogram in Fig. 4(b) gives the distribution of the ob-
 283 jective function residuals for 100 accepted configurations and verifies that all
 284 of them correspond to small ($< 2 \times 10^{-4}$) values.

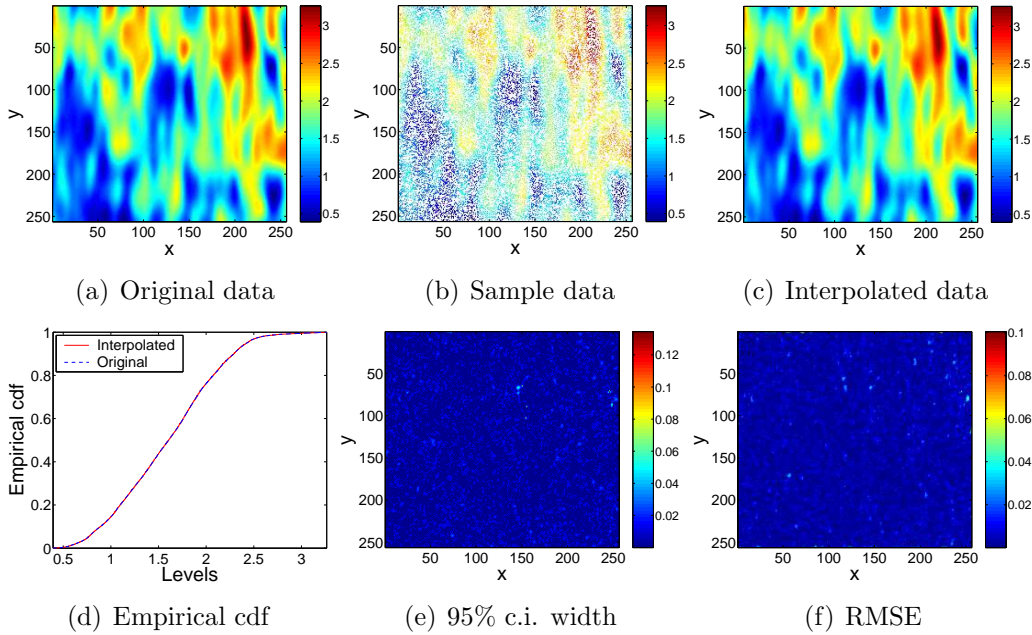


Figure 3: DGC interpolation of the radioactivity data obtained from $M = 100$ simulation runs using one sample set generated by 66% thinning. The plots are as those in Fig. 1.

Table 3: Classification ($N_c = 8, 16$) and interpolation ($N_c = 1500$) results for the radioactivity data with $p = 33\%$ thinning. DGC is compared with k-nearest neighbor (KNN) and fuzzy k-nearest neighbor (FKNN) models for classifications, and with the nearest neighbor (NN), bilinear (BL), bicubic (BC), biharmonic spline (BS) and inverse distance (ID) models for interpolation.

Model	Classification				Interpolation					
	$N_c = 8$		$N_c = 16$		$N_c = 1500$					
	$\langle F^* \rangle$	S_{F^*}	$\langle F^* \rangle$	S_{F^*}	MAAE	MARE [%]	MAARE [%]	MRASE	MR [%]	$\langle T_{cpu} \rangle$
DGC	4.01	0.21	8.64	0.28	$9.4e-4$	$-2.2e-3$	$6.8e-2$	$1.56e-3$	100.00	39.94
KNN	4.96	0.16	11.44	0.22	-	-	-	-	-	-
FKNN	4.22	0.16	10.14	0.23	-	-	-	-	-	-
NN	-	-	-	-	$2.3e-2$	-0.165	1.64	$3.5e-2$	99.78	1.41
BL	-	-	-	-	$3.7e-3$	$-5.9e-2$	0.27	$5.9e-3$	99.78	1.40
BC	-	-	-	-	$1.7e-3$	$-2.2e-2$	0.12	$2.9e-3$	100.00	1.46
BS	-	-	-	-	$4.7e-4$	$-1.2e-3$	$3.4e-2$	$7.6e-4$	100.00	32.82
ID	-	-	-	-	$1.3e-2$	-0.160	0.90	$1.7e-2$	99.95	183.64

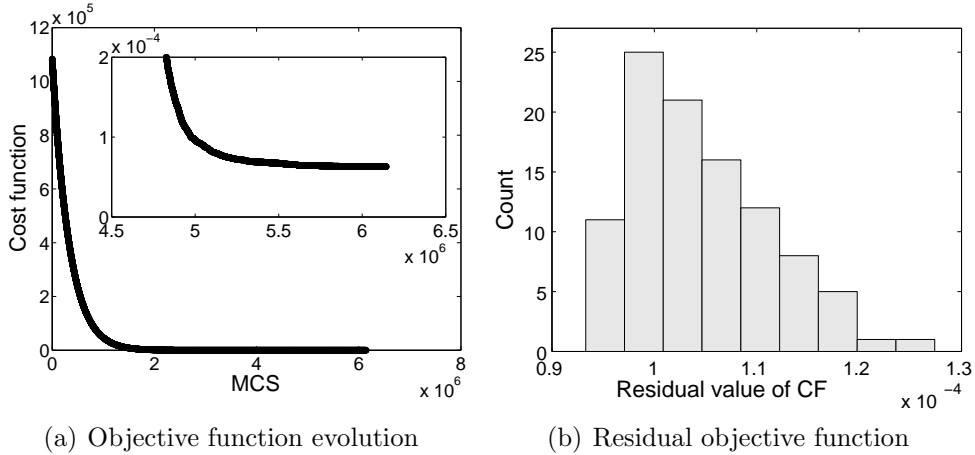


Figure 4: Left: Evolution of the objective (cost) function (3) for potassium concentration versus the number of Monte Carlo steps. Inset focuses on the convergence to the optimum. Right: Histogram of the objective function residual values obtained from 100 different runs.

285 4.2.2. Ozone Layer Thickness

286 The second real-world data set represents daily column ozone measure-
 287 ments on June 1, 2007 (Acker and Leptoukh, 2007). The data are on a
 288 $1^\circ \times 1^\circ$ grid with $N_G = 180 \times 360$ nodes extending in latitude from 90S
 289 to 90N and in longitude from 180W to 180E. The data set includes natu-
 290 rally missing (and therefore unknown) values. The data are in Dobson units
 291 with the following summary statistics: $N = 48501$, $z_{\min} = 158$, $z_{\max} = 596$,
 292 $\bar{z} = 311.58$, $z_{0.50} = 308$, $\sigma_z = 46.05$, skewness coefficient equal to 0.31, and
 293 kurtosis coefficient equal to 2.30. The gaps are mainly due to limited cov-
 294 erage on the particular day, generating conspicuous stripes of missing values
 295 in the south-north direction. Since the true values at these locations are
 296 not known, validation measures are not evaluated. Instead, the interpolation
 297 quality is assessed empirically, based on the visual continuity between the

298 observed data and the predictions.

299 In the DGC reconstructed image, as shown in Fig. 5(b), some traces of
 300 the stripe pattern due to overestimation in low-value areas (averaging effect)
 301 can still be observed. However, this effect is somewhat less pronounced than
 302 in other interpolation methods, presented in Fig. 6. Indeed, histograms of
 303 the predicted values, see Fig. 7, show a larger proportion of DGC predictions
 304 in bins below the sample average $\bar{z} = 311.58$ compared to the other methods.

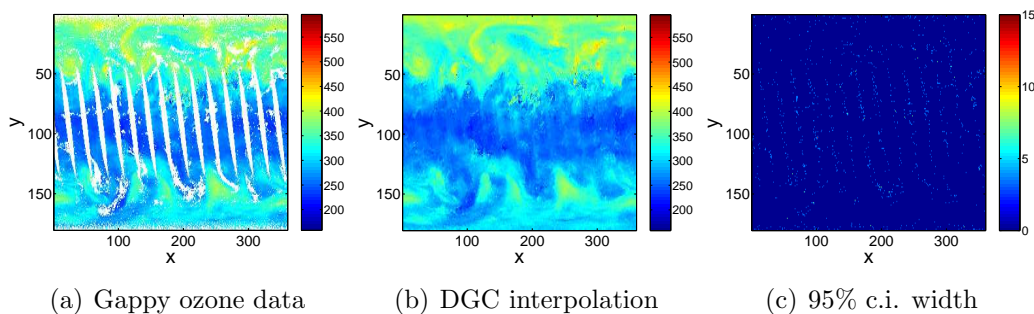


Figure 5: DGC interpolation results for ozone data, obtained from $M = 100$ simulation runs on one set of the original data with missing values: Original data (a), interpolated data based on the median values from M runs (b), and spatial distribution of the 95% confidence interval (c.i.) widths (c).

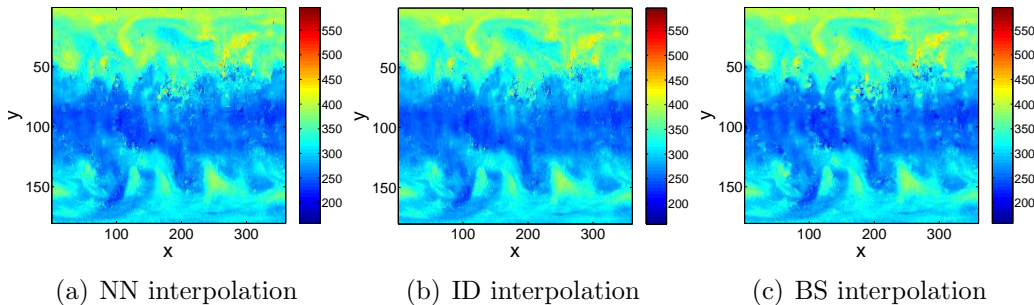


Figure 6: Interpolation results for ozone data, using the nearest-neighbor (NN) (a), the inverse distance (ID) (b), and the biharmonic spline (BS) (c) methods.

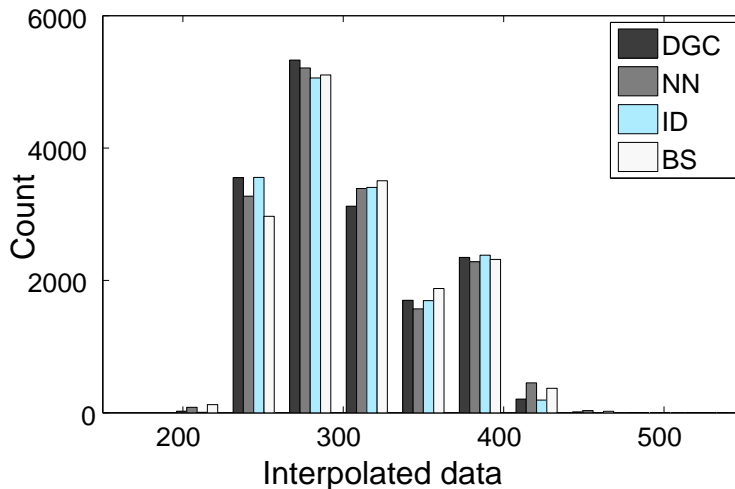


Figure 7: Histograms of the ozone values predicted by the respective methods: DGC, NN, ID, and BS.

305 5. Discussion and Conclusions

306 We presented and investigated the DGC method for the prediction of
 307 missing data on rectangular grids. DGC is based on stochastic simulation
 308 conditioned by sample data with a global objective function that accounts
 309 for anisotropic correlations. The constraints involve normalized directional
 310 gradient and curvature energies in specified directions. The simulation sam-
 311 ples the configuration subspace that leads to local minima of the objective
 312 function.

313 For reliable application of DGC sufficiently high sampling density and
 314 number of data for the calculation of sample constraints are desirable. We
 315 evaluated the average numbers n_p of nearest-neighbor sampling-point pairs
 316 per direction and n_t of compact triplets of sampling points per direction. The

317 first, n_p , is equal to the number of terms involved in $\overline{G}_n(\mathbf{I}_s)$, while the second,
 318 n_t , is the number of terms in $\overline{C}_n(\mathbf{I}_s)$. For uniform random thinning n_p and n_t
 319 depend only on the degree of thinning p and the domain size L . For $p = 66\%$
 320 we obtained $(n_p, n_t) = (280, 92)$ for $L = 50$ and $(n_p, n_t) = (7523, 2542)$ for
 321 $L = 256$ without significant differences between different directions. These
 322 values are sufficient for reliable estimates of $\overline{G}_n(\mathbf{I}_s)$ and $\overline{C}_n(\mathbf{I}_s)$. However,
 323 smaller grids or higher thinning degrees can lead to insufficient sampling.

324 Regarding sensitivity of DGC to noise, we have run tests on simulated
 325 random field realizations to which Gaussian white noise is added. DGC seems
 326 more sensitive to noise than other interpolation methods (e.g., BL, BC, BS),
 327 resulting in a larger increase of cross-validation errors with increasing noise
 328 variance. This effect is caused by the fact that methods like BL, BC, and BS
 329 perform some smoothing of the noise by means of the weighted average over
 330 extended neighbors. DGC on the other hand focuses on correlations over a
 331 small local neighborhood, which are sensitive to noise. Hence, in its current
 332 formulation DGC is more useful for smooth data distributions, such as the
 333 ones studied herein. For noisy data, improvements can be made by developing
 334 directional kernel-based estimators for the square gradient and curvature in
 335 the spirit of (Elogne & Hristopulos, 2008; Hristopulos & Elogne, 2009) or by
 336 incorporating an initial filtering stage to reduce noise (Brownrigg, 1984; Yin,
 337 1996).

338 DGC does not rely on assumptions about the probability distribution of
 339 the data, it is reasonably efficient computationally, and it requires very little
 340 user input (i.e., the number of simulation runs, the number of class levels and
 341 the size of the maximum stencil for initial state selection). Potential applica-

342 tions include filling of data gaps in satellite images and restoration of dam-
343 aged digital records. For applications in the interpolation of data sampled on
344 an irregular grid, DGC needs to be extended to account for the lack of grid
345 structure. This can be accomplished using kernel functions with adjustable
346 bandwidth as shown in (Elogne & Hristopulos, 2008; Hristopulos & Elogne,
347 2009).

348 DGC shares conceptual similarities with interpolation methods based on
349 splines, which are generated by minimizing an objective function formed
350 by the linear combination of the square gradient and the square curva-
351 ture (Wessel, 2009). A special case of the splines-based approach is the
352 BS method used above for comparison purposes. DGC does not require min-
353 imization of the square gradient and curvature but requires matching the
354 sample and entire-grid values of these constraints. Splines-based methods
355 require solving a linear system involving the Green’s function of the interpo-
356 lation operator; the numerical complexity of this calculation scales with the
357 third power of the system size. DGC does not require such a costly operation,
358 because the objective functional is defined using local couplings. Finally, in
359 contrast with splines interpolation, DGC introduces a stochastic element by
360 sampling the configuration subspace of local minima of the DGC objective
361 function. On the other hand, splines-based methods can handle irregularly
362 spaced samples, while DGC is currently restricted to grid data.

363 **Acknowledgments**

364 This work is funded by the European Commission, under the 6th Frame-
365 work Programme, Contract N. 033811, DG INFSO, action Line IST-2005-

366 2.5.12 ICT for Environmental Risk Management. The views expressed herein
367 are those of the authors and not necessarily those of the European Commis-
368 sion.

369 Ozone layer thickness data used in this paper were produced with the Gio-
370 vanni online data system, developed and maintained by the NASA Goddard
371 Earth Sciences (GES) Data and Information Services Center (DISC).

372 **References**

373 **References**

374 Acker, J.G., Leptoukh, G., 2007. Online Analysis Enhances of NASA Earth
375 Science Data, Eos, Trans. AGU, Vol. 88, No. 2 (9 January 2007), 14-17.
376 Online at: <http://disc.sci.gsfc.nasa.gov/giovanni/>

377 Akbas, E., 2007. Fuzzy k-NN (<http://www.mathworks.com/matlabcentral/fileexchange/13358-fuzzy>),
378 MATLAB Central File Exchange. Retrieved August 10, 2008.

379 Albert, M.F.M.A., Schaap, M., Manders, A.M.M., Scannell, C. , O'Dowd,
380 C.D. , de Leeuw, G., 2012. Uncertainties in the determination of global
381 sub-micron marine organic matter emissions. Atmospheric Environment,
382 57(9), 289-300.

383 Anonymous, 2008. National Gamma-Ray Spectrometry Data Base, Geo-
384 science Data Repository, Geological Survey of Canada, Earth Sciences
385 Sector, Natural Resources Canada, Government of Canada. Online at:
386 <http://www.nrcan.gc.ca/earth-sciences/home>

- 387 Bechle, M.J., Millet, D.B., Marshall, J.D. Remote sensing of exposure
388 to NO₂: satellite versus ground based measurement in a large urban
389 area. *Atmospheric Environment*, Available online 13 December 2012, doi:
390 10.1016/j.atmosenv.2012.11.046.
- 391 Brownrigg, D.R.K., 1984. The weighted median filter. *ACM Communica-*
392 *tions*, 27(8), 807-818.
- 393 Cressie, N., 2008. Fixed rank kriging for very large spatial data sets. *Journal*
394 *of the Royal Statistical Society Series B*, 70(1), 209-226.
- 395 Dasarathy, B.V. (Ed.), 1991. Nearest neighbor norms: NN pattern classifi-
396 cation techniques. IEEE Computer Society Press, Los Alamitos, CA.
- 397 Diggle, P.J., Ribeiro, Jr., P.J., 2007. *Model-based Geostatistics. Series:*
398 *Springer series in statistics*. Springer, New York.
- 399 Drummond, I.T., Horgan, R.R., 1987. The effective permeability of a random
400 medium. *Journal of Physics A*, 20, 4661-4672.
- 401 Elogne S.N., Hristopulos D.T., 2008. Geostatistical applications of Spartan
402 spatial random fields. In: *Proceedings of the 6th International Conference*
403 *on Geostatistics for Environmental Applications*, Rhodes, Greece: October
404 2006. Eds. A. Soares and M.J. Pereira and R. Dimitrakopoulos, Vol. 15,
405 pp. 477-488, Springer, Berlin.
- 406 Emili, E., Popp, C., Wunderle, S., Zebisch, M., Petitta, M., 2011. Map-
407 ping particulate matter in alpine regions with satellite and ground-based
408 measurements: An exploratory study for data assimilation. *Atmospheric*
409 *Environment*, 45(26), 4344-4353.

- 410 Hartman, L., Hössjer, O., 2008. Fast kriging of large data sets with Gaussian
411 Markov random fields. *Computational Statistics and Data Analysis*, 52,
412 2331 - 2349.
- 413 Howat, I.M., 2007. Filling NaNs in array using inverse-distance weighting.
414 (<http://www.mathworks.com/matlabcentral/fileexchange/15590-fillnans>),
415 MATLAB Central File Exchange. Retrieved June 15, 2009.
- 416 Hristopulos, D.T., 2003. Spartan Gibbs random field models for geostatistical
417 applications, *SIAM Journal in Scientific Computation*, 24, 2125-2162.
- 418 Hristopulos, D.T., Elogne, S.N., 2009. Computationally efficient spatial inter-
419 polators based on Spartan spatial random fields, *SIAM Journal in Scientific*
420 *Computation*, 57(9), 3475-3487.
- 421 Jun, M., Stein, M.L., 2004. Statistical comparison of observed and CMAQ
422 modeled daily sulfate levels. *Atmospheric Environment*, 38(27), 4427-4436.
- 423 Junninen, H., Niska, H., Tuppurainen, K., Ruuskanen, J., Kolehmainen, M.,
424 2004. Methods for imputation of missing values in air quality data sets.
425 *Atmospheric Environment*, 38(18), 2895-2907.
- 426 Keller, J.M., Gray, M.R., Givens, J.A.Jr., 1985. Fuzzy k-nearest neighbor
427 algorithm. *IEEE Transactions on Systems, Man and Cybernetics*, 15, 580-
428 585.
- 429 Lehman, J., Swinton, K., Bortnick, S., Hamilton, C., Baldrige, E., Eder,
430 B., Cox, B. 2004. Spatio-temporal characterization of tropospheric ozone
431 across the eastern United States. *Atmospheric Environment*, 38(26), 4357-
432 4369.

- 433 Papadimitriou, C.H., Steiglitz, K., 1982. *Combinatorial Optimization*. Pren-
434 tice Hall, New Jersey.
- 435 Sandwell, D.T., 1987. Biharmonic Spline Interpolation of GEOS-3 and
436 SEASAT Altimeter Data. *Geophysical Research Letters*, 14, 139-142.
- 437 Shepard, D., 1968. A two-dimensional interpolation function for irregularly-
438 spaced data. Proceedings of the 1968 ACM National Conference, 517-524.
- 439 Sickles, J.E., Shadwick, D.S., 2007. Effects of missing seasonal data on esti-
440 mates of period means of dry and wet deposition. *Atmospheric Environ-*
441 *ment*, 41(23), 4931-4939.
- 442 Sidler, R., 2009. vebyk: Value Estimation BY Kriging.
443 (<http://www.mathworks.com/matlabcentral/fileexchange/4566-vebyk>),
444 MATLAB Central File Exchange. Retrieved June 15, 2009.
- 445 Wackernagel, H., 2003. *Multivariate Geostatistics*. Springer, New York.
- 446 Wessel, P., 2009. A general-purpose Green's function-based interpolator.
447 *Computers & Geosciences*, 35(6), 1247-1254.
- 448 Yin, L., Yang, R.K., Gabbouj, M., Neuvo, Y., 1996. Weighted median filters:
449 A tutorial. *IEEE Transactions on Circuits and Systems II*, 43(3), 157192.
- 450 Žukovič, M., Hristopulos D.T., 2012. Reconstruction of missing data in re-
451 mote sensing images using conditional stochastic optimization with global
452 geometric constraints, *Stoch Environ Res Risk Assess*, Available online 4
453 Spetember 2012, doi: 10.1007/s00477-012-0618-5.